ROYAL SOCIETY OF CHEMISTRY

Check for updates

Modeling secondary organic aerosols from β-caryophyllene: role of extremely low-volatile organic compounds on new particle formation and evaluation of the SOA composition

Yijie Shi, [ID] *[ab] Florian Couvidat,*[a] Victor Lannuque[a] and Karine Sartelet [ID] [b]

β-Caryophyllene (BCARY), a prevalent biogenic sesquiterpene, is an important precursor of secondary organic aerosol (SOA). While extremely low-volatility organic compounds (ELVOCs) formation by autoxidation may be critical to accurately represent SOA formation, current mechanisms omit this process. To address this missing process, we developed the autoX-MCM mechanism as an extension of the Master Chemical Mechanism v3.3.1 by incorporating a semi-explicit peroxy radical autoxidation for BCARY ozonolysis and oxidation by the nitrate radical ($NO_3^{\bullet}$). The mechanism was constrained against a suite of literature experiments conducted in both flow-tube and chamber reactors. Simulation using SSH-aerosol with autoX-MCM successfully reproduced ELVOC yields, SOA mass loading, and new particle formation reported by several experimental studies at different temperatures (from 273 K to 313 K). The developed mechanism also simulated accurately SOA composition, including β-caryophyllinic acid yields, the amount of oligomers, and the amount of SOA containing a nitrate group. Our results indicate that including autoxidation in the BCARY oxidation mechanism is essential to accurately reproduce SOA formation, especially at 298 K, the model reproduced SOA concentrations with a mean bias of 0.05 μg m^{-3} and a normalized RMSE of 3.89% compared with experimental observation.

Environmental significance

Due to the impact of particles on health and climate change, models have been developed to simulate particle concentrations. Organic aerosols contribute by around 20 to 80% to particle concentrations but representing secondary organic aerosols (SOA) remain challenging. β-Caryophyllene is an important biogenic precursor of secondary organic aerosol (SOA), yet its oxidation mechanisms remain incomplete, limiting our ability to accurately simulate SOA and new particle formation. This study presents a new mechanism that represents extremely low-volatile organic compound (ELVOC) formation from β-caryophyllene oxidation. Implementing ELVOC improves the simulation of particle number concentrations, SOA concentrations and composition. These findings highlight the importance of autoxidation in the β-caryophyllene chemistry that should be taken in models to simulate new particle and SOA formation.

1 Introduction

Sesquiterpenes (SQTs, with the chemical formula $C_{15}H_{24}$) are a class of biogenic volatile organic compounds (BVOCs) and known precursors of secondary organic aerosol (SOA). While their global emissions are lower than those of lighter BVOCs such as isoprene and monoterpenes, estimated at 3% *versus* about 50% and 15%, respectively[1] of the total global BVOC emission, SQTs contribute to SOA formation,[2–4] with high SOA yields (20–80%) observed under typical temperatures (273–313 K).[5,6] Several modeling studies using 3D air quality models report a large contribution of SQTs to SOA formation: *e.g.* 6% of

SOA in Amazonia reported by Shrivastava *et al.*,[7] 12–35% of SOA in southeast Texas reported by Zhang and Ying,[8] 27.8% of the global SOA budget by Khan *et al.*[9] However, all these estimations highly depend on the SOA mechanism used. β-Caryophyllene (BCARY) is a highly reactive SQT[10–12] frequently used as a surrogate for SQTs in atmospheric modeling studies. Although this compound may not be representative of all SQTS,[13] BCARY chemistry was investigated in numerous experimental studies,[6,9,14–17] making this compound a valuable reference molecule for mechanism development and model evaluation. Therefore, a detailed understanding of BCARY SOA formation mechanisms is essential to improve the accuracy of atmospheric aerosol modeling and for characterizing the broader role of BVOCs on air quality.

Current mechanisms used in 3-D air quality models for BCARY SOA formation are generally very simplified and do not represent all the complexity of BCARY chemistry. The oxidation

[a]Institut National de l'Environnement Industriel et des Risques, INERIS, 60 550 Verneuil en Halatte, France. E-mail: Yijie.SHI@ineris.fr; Florian.COUVIDAT@ineris.fr
[b]CEREA, ENPC, Institut Polytechnique de Paris, EdF R&D, IPSL, 77 455 Marne la Vallée, France

of BCARY in the atmosphere is initiated by reactions with major oxidants such as O_3, the hydroxyl radical ($\dot{O}H$), and the nitrate radical ($NO_3^\cdot$). These initial oxidation reactions produce organic peroxy radicals ($RO_2^\cdot$), which can engage in bimolecular reactions with NO, $NO_3^\cdot$, $HO_2^\cdot$, or other $RO_2^\cdot$ species and therefore lead to SOA formation in different amounts according to the chemical pathways. Additionally, recent studies suggested that $RO_2^\cdot$ formed by the oxidation of monoterpenes can undergo autoxidation by successive intramolecular hydrogen shift (H-shift) reactions, forming highly oxygenated molecules (HOMs).[18] However, no studies focused on the importance of the autoxidation pathway in SOA formation from BCARY. The importance of this process should therefore be investigated.

The BCARY oxidation products often retain a long carbon skeleton and possess multiple functional groups (i.e., hydroperoxides, peroxy acids, ketones, and alcohols), resulting in very low saturation vapor pressures and extremely low-volatility organic compounds (ELVOCs) formation potential. ELVOCs (considered as compounds with vapor pressures below 1.0×10^{-10} torr) readily partition into the particle phase and play a central role in secondary organic aerosol (SOA) and new particle formation and growth.[12,19–22] Experimental studies have confirmed the formation of ELVOCs from BCARY oxidation. Notably, Gao et al.,[6] Jokinen et al.,[14] Richters et al.[15,16] showed that compounds like $C_{14-15}H_{23-25}O_{7-10}$ dominate the ELVOC concentrations formed from the oxidation of BCARY.

An accurate representation of autoxidation is therefore essential for modeling SOA formation from BCARY. The Master Chemical Mechanism v3.3.1 (MCM) provides a near-explicit and comprehensive representation of the atmospheric gas-phase chemistry of BCARY. However, the current MCM version does not consider the autoxidation pathways responsible for ELVOC formation.

Recent advances in the modeling of other BVOCs, such as α-pinene and isoprene, have shown that explicitly incorporating ELVOC formation by autoxidation improves SOA modeling.[19,23,24] Moreover, Roldin et al.[21] and Sengupta et al.[25] demonstrated that including HOM formation by autoxidation improved the simulation of new particle formation. These studies underline the importance of mechanisms representing ELVOC formation pathways for improving the predictive accuracy of atmospheric models.

The current study aims to improve the simulation of SOA formation from the oxidation of β-caryophyllene by ozone and nitrate. A new parameterized autoxidation mechanism (autoX-MCM) was developed to represent the formation of ELVOCs from BCARY-derived SOA formation and was combined with the current MCM gas-phase oxidation mechanism. The different parameters of the mechanism were constrained to reproduce the amount of ELVOC reported by different chamber experiments. The results of the developed mechanism were evaluated by comparison to the chamber experiments of Gao et al.[6] The study details the development of the new mechanism, including updates to the oxidation pathways and model implementation and presents comparisons with different laboratory experiments and sensitivity analyses.

2 Methodology

The ELVOC mechanism developed in this study was implemented in the 0-D aerosol formation model SSH-aerosol v2.0 (ref. 26 and 27) to simulate SOA and particle number concentrations from BCARY oxidation. Several parameters of the developed mechanism were fitted to data on ELVOC formation from experimental studies performed in oxidation reactors from several groups and covering different conditions.[6,14–16] The mechanism performance was evaluated by comparison with the chamber study results of Gao et al.[6] at different temperatures. In order to simulate concentrations of chamber experiments accurately, wall losses of gases and particles were taken into consideration. The two mechanisms for BCARY SOA formation (based on the MCM mechanism with and without autoxidation) are first presented in this section, followed by a description of the model framework and simulation set-up used to optimize the unknown parameters in the developed mechanisms.

2.1 Coupling of MCMv3.3.1 with CB05 ('mMCM')

The first mechanism, referred to as 'mMCM' in this study, was constructed by merging MCMv3.3.1 and CB05. MCMv3.3.1 provides an explicit description of the gas-phase oxidation of BCARY and its intermediates, offering a detailed chemical basis for investigating BCARY-derived SOA formation. However, the BCARY oxidation process also involves the participation of inorganic radical and oxidants such as $NO_3^\cdot$ and O_3. In order to account for the influence of inorganic gases on radicals and therefore on SOA formation, the part of the CB05 mechanism[28] not concerning BCARY was used.

Finally, the mMCM mechanism contains 1220 reactions and 562 species, including 325 condensable compounds (with 13 species classified as ELVOCs), and 119 $RO_2^\cdot$, ref. 28 and 29.

2.2 Developed mechanism including autoxidation ('autoX-MCM')

The second chemical mechanism used in this study, hereafter referred to as autoX-MCM, was built upon mMCM by incorporating a simplified mechanism for the formation of ELVOCs resulting from the oxidation of BCARY by O_3 and $NO_3^\cdot$. While autoxidation is a key process in SOA formation, it is not represented in the original mMCM. To address this, the mMCM mechanism was modified to include ELVOC formation processes.

Due to limited experimental observations (on yields and kinetic rates) and an incomplete understanding of autoxidation pathways, the development of a fully explicit mechanism able to reproduce ELVOC formation from chamber studies is currently difficult. Therefore, following the approach of Chrit et al.,[24] a simplified mechanism was constructed to consider the major chemical pathways involved in ELVOC formation. This simplified mechanism includes only the main reactions and representative species relevant to ELVOC formation from BCARY oxidation. The unknown parameters were constrained by fitting the model to available experimental data.[6,14,16] This approach allowed for the development of a practical and reliable

mechanism without sacrificing critical insights into ELVOC formation.

Fig. 6 and 7 present schematic overviews of the O_3- and NO_3-initiated BCARY oxidation mechanisms included in autoX-MCM, with optimized parameters highlighted in red. For clarity and completeness, detailed reaction pathways, intermediate species, and branching logic for both oxidation routes are provided in the SI (Section S1).

The key processes introduced in autoX-MCM include H-shift reactions, as well as bimolecular reactions involving peroxy radicals: $RO_2 + NO + RO_2 + NO_3 + RO_2 + HO_2$ and $RO_2 + RO_2$. In this mechanism, specific molar yields were assigned to the initial RO_2 radicals that start the autoxidation chains (see Table S1). These yields (γ and η shown in Fig. 6 and 7) provided an upper-bound estimate of ELVOC production from the various oxidation pathways.

Regarding reaction kinetics, autoX-MCM adopts the same rate constants as MCMv3.3.1 for RO_2 reactions with NO, NO_3, and HO_2. The rate coefficients for H-shift reactions and $RO_2 + RO_2$ termination reactions were optimized by fitting to experimental results and are summarized in SI Table S1.

AutoX-MCM differentiates the resulting products based on the specific oxidant involved. In total, autoX-MCM introduces 15 new species: 7 for ozonolysis and 9 for the oxidation by NO_3. A general theoretical overview of autoX-MCM is provided in the following subsections. Properties of species are available in the Zenodo repository (see section "Data availability").

In the autoX-MCM, autoxidation proceeds through a propagation sequence of intramolecular H-shift reactions and subsequent O_2 additions. The resulting peroxy radicals can then undergo termination via bimolecular reactions with species such as HO_2, NO, NO_3, or RO_2. When two RO_2 radicals react, they can form either stable functionalized monomers or dimers.

Since the simulations correspond to dark experimental conditions, only the oxidation of BCARY by O_3 and NO_3 was considered. Moreover, the most important oxidants of BCARY are likely to be O_3 and NO_3. Indeed, based on the MCM kinetics at 298 K, the kinetic rate parameters with O_3 and OH are equal to 1.2×10^{-14} molecules^{-1} cm^{-3} s^{-1} and 1.97×10^{-10} molecules^{-1} cm^{-3} s^{-1}, respectively. Using a background O_3 concentration of 7×10^{11} molecules cm^{-3} (around 35 ppb) and a concentration of 1×10^6 molecules cm^{-3} for OH, it can be estimated that almost all BCARY (around 98%) should react with O_3. Moreover, based on previously simulated results with the air quality model CHIMERE by Lanzafame et al.,[30] we estimated that, on average over Europe in summer, approximately 97% of BCARY reacts with O_3 during daytime and that the fraction reacting with OH rarely exceeds 6%.

In the autoX-MCM, the structures of the formed SOA compounds by autoxidation were selected based on the type of reactions leading to their formation (e.g., $RO_2 + HO_2$ reactions lead to the formation of hydroperoxides). For simplification purposes, it was assumed that all the formed compounds by autoxidation preserve the complete C_{15} skeleton. To capture the dominant chemical processes while maintaining computational efficiency, the model only resolved the autoxidation pathways originating from the oxidant attack on the endocyclic

double bond. As the reaction of O_3 on the exocyclic double bond is slower,[10] it is not represented in mMCM and autoX-MCM.

2.3 Parameter optimization of the autoX-MCM

2.3.1 Parameter selection. The core of the autoX-MCM development involved constraining a set of key parameters that govern the whole autoxidation process. Three categories of parameters were identified as most critical for accurately representing the formation of ELVOCs and subsequent SOA production:

• The initial branching ratio (γ): The yield of the BCALAO2 in reaction R_0 determines the total flux of molecules entering the autoxidation pathway. This branching ratio directly influences the initiation of the peroxy radical chain that leads to multi-generation oxidation products.

• The intramolecular H-shift rate constants (k_{1a} and k_{1b}): These parameters control how quickly autoxidation occurs.

• $RO_2 + RO_2$ termination rate constants ((k_5, k_6, k_7, and k_8): These bimolecular reactions compete with the autoxidation reactions and end the propagation process by forming the stable compounds.

Constraining these seven parameters was essential, as they remained experimentally uncharacterized.

2.3.2 Experimental datasets for mechanism development and validation. To optimize the seven parameters of autoX-MCM, a set of laboratory experiments was selected to provide robust constraints across varying chemical regimes, residence times, and detection techniques (Tables 1 and 2). The experimental cases could be broadly categorized into flow-tube and chamber experiments.

Several flow-tube experiments (Cases 1–3) were selected from Jokinen et al.[14] and Richters et al.[16] These experiments featured short residence times (7.9–18 s) and a single oxidant design (BCARY + O_3), offering ideal conditions for studying the initial oxidation steps of BCARY, before aerosol processes like condensation and coagulation occur. Because aerosol formation is negligible on such short timescales, species are directly measured within the gas-phase, particularly the formation of ELVOCs. Importantly, these experiments employed different reagent ion chemistry in the chemical ionization—atmospheric pressure interface – time-of-flight (CI-APi-TOF) mass spectrometry, which significantly affected the detection sensitivity to specific oxidation products. For instance, Cases 1 and 2 used nitrate ionization, favoring the detection of highly oxygenated compounds such as $C_{15}H_{24}O_8$, whereas Case 3 used acetate ionization, which significantly enhanced signals for less oxygenated monomeric compounds like $C_{15}H_{24}O_6$.

From a volatility perspective, $C_{15}H_{24}O_6$ exhibits a P_{sat} (7.9×10^{-9}, estimated by the 'v0b0' method, detailed in Section 2.4.1) greater than 1.0×10^{-10} torr. Consequently, it does not meet the criteria of an ELVOC (detailed in Section 2.4.1). In order to distinguish the ELVOC yield (compounds with P_{sat} less than 1.0×10^{-10} torr) from the yield of ELVOC + $C_{15}H_{24}O_6$, the term 'ELVOC$^+$' was adopted.

In addition to the flow-tube experiments, a shortened chamber case (Case 4) was extracted from Gao et al.[6] (Case 5).

Table 1 Compilation of experimental conditions used in model configuration. Precursors: BCARY + O_3

Ref.	Cases no.	Light	T (K)	RH (%)	Residence time	BCARY ($\mu g\ m^{-3}$)	O_3 (ppb)	OH scavenging
Jokinen et al.[14]	1	Dark	294	10	18.0 s	144.0	18.0	—
Richters et al.[16]	2	Dark	297	0.1	7.9 s	28.16	41.27	Alkane
Richters et al.[16]	3	Dark	297	0.1	7.9 s	29.18	41.27	Alkane
Gao et al.[6]	4	Dark	298	27	11.5 min	65.0	25.0	—

Case 4 represents only the first minutes (16.5 min) of Case 5 in order to target SOA growth during a period strongly driven by ELVOC and new particle formation.

By contrast, the full chamber experiments (Cases 5–7) were conducted over longer residence times (several hours), enabling the evaluation of the mechanism over relevant timescales. These cases were selected from the chamber experiments of Gao et al.,[6] and span different temperatures (273–313 K). These chamber experiments were divided into several stages corresponding to the new injection of reactants (BCARY, O_3, or NO_2 that lead to the formation of $NO_3^{\cdot}$) during the experiments. These experiments can be used to evaluate both the BCARY + O_3 and BCARY + $NO_3^{\cdot}$ mechanisms, making them suitable for validating the mechanism under a variety of environmental conditions. Compared with flow-tube studies, chamber experiments additionally capture several processes such as gas–particle partitioning, nucleation, coagulation, and aging, thus allowing for more comprehensive model evaluation.

Together, these two types of experiments formed a complementary dataset for parameterizing and validating the BCARY autoxidation mechanism, covering both gas-phase chemical evolution and SOA formation dynamics. If we had attempted to develop and constrain the autoxidation mechanism using only chamber experiments, the model would have underestimated the initial ELVOC production. This is because, in the absence of seed particles, ELVOC formation greatly influences SOA and new particle in the early stage of the BCARY oxidation. In our study, using both experimental types allowed us to capture both the fast autoxidation chemistry and the slower SOA evolution processes, leading to a more robust and generalizable mechanism.

2.3.3 Experimental constraints and parameter optimization. To constrain the above parameters shown in Section 2.3.1, an error function was constructed to guide the parameter optimization, reducing the deviation between model outputs and selected experimental targets. The optimization relied on both flow-tube and chamber experiments, and the constraints were summarized in Table 3, including ELVOC (or ELVOC$^+$) yields and SOA volume concentrations, along with the specific species included for each case:

• Case 1:[14] dominant signals detected by nitrate ionization included extremely low-volatile monomers (e.g., $C_{15}H_{24}O_8$) and dimers (e.g., $C_{30}H_{47}O_8$). Based on these observations, two new compounds were included in the simulated ELVOC yield.

• Case 2:[16] due to the lack of dimer detection, only monomeric ELVOCs were included. Primary signal detected by nitrate ionization was $C_{15}H_{24}O_8$.

• Case 3:[16] the signal of $C_{15}H_{24}O_6$ increased by an order of magnitude under acetate detection, while $C_{15}H_{24}O_8$ remained nearly unchanged. Although $C_{15}H_{24}O_6$ possesses a higher P_{sat} ('v0b0' method), its significant response to detection and crucial role in constraining the mechanism necessitate its inclusion in the yield calculations for this specific case. Therefore, in this context, one low-volatile monomer ($C_{15}H_{24}O_6$) and one ELVOC ($C_{15}H_{24}O_8$) were included for the ELVOC$^+$ yield calculation, with all dimeric species excluded.

• Case 4[6] was used to constrain the SOA formation during BCARY + O_3 mechanism. The SOA volume concentration was derived from Scanning Mobility Particle Sizer (SMPS) measurements, as described in Section 2.5.

Notably, the autoX-MCM was developed by extending the base mechanism mMCM. Thus, the calculated ELVOC (or ELVOC$^+$) yields also include 13 ELVOC species inherited from mMCM in the optimization.

The seven unknown parameters in autoX-MCM were constrained by minimizing the total error between model simulations and experimental observations of ELVOC yields and SOA volume concentrations. In addition, for the BCARY + $NO_3^{\cdot}$

Table 2 Experimental conditions and the amount of reactants injected in the chamber of Gao et al.[6] at the different stages of the experiments. No light and an OH scavenger were used in the chamber experiments. The unit of BCARY concentration is $\mu g\ m^{-3}$, and those of O_3 and NO_2 are ppb. The total uncertainty in BCARY quantification was estimated to be $\pm20\%$ by Gao et al.[6]

Cases no.	T (K)	RH (%)	Residence time (min)	1st	2nd	Gas injection 3rd[a]	4th	5th
5	298	27	230	BCARY: $65^{+13.0}_{-13.0}$	—	BCARY: $23.2^{+4.6}_{-4.6}$	—	BCARY: $27.9^{+5.6}_{-5.6}$
				O_3: 25	O_3: to 315	—	NO_2: 42	—
6	273	67	250	BCARY: $109.5^{+21.9}_{-21.9}$	—	—	BCARY: $109.5^{+21.9}_{-21.9}$	—
				O_3: 73	NO_2: 42	O_3: to 290	—	—
7	313	13	120	BCARY: $78.6^{+15.7}_{-15.7}$	—	—	BCARY: $24.6^{+4.9}_{-4.9}$	—
				O_3: 25	O_3: to 270	NO_2: 42	—	—

[a] The times of gas injections were different among the three cases.

Table 3 Experimental constraints used for autoX-MCM optimization and a comparison of the calculated yields or volume concentrations between the mMCM and the optimized autoX-MCM mechanisms

Cases no.	Constraints	Involved species	mMCM	autoX-MCM
1	ELVOC yield: $1.70^{+1.28}_{-1.28}$%	$C_{15}H_{24}O_8$, $C_{30}H_{47}O_8$, and 13 ELVOCs in 'mMCM'	0.0001%	1.17%
2	ELVOC yield: $0.37^{+0.5}_{-0.3}$%	$C_{15}H_{24}O_8$ and 13 ELVOCs in 'mMCM'	0.00%	0.46%
3	ELVOC + yield^a: $1.37^{+1.8}_{-0.9}$%	$C_{15}H_{24}O_6$, $C_{15}H_{24}O_8$, and 13 ELVOCs in 'mMCM'	0.192%	1.36%
4	SOA volume concentration: $6.47^{+1.29}_{-1.29}$ nL m^{-3}	all condensable species in autoX-MCM	1.06 nL m^{-3}	6.48 nL m^{-3}

^{a} ELVOC$^+$ is calculated as the sum of $C_{15}H_{24}O_6$ (not classified as an ELVOC) and the other ELVOCs. See Section 2.3.3 for detailed definitions of ELVOC and ELVOC$^+$.

mechanism, several key unknown parameters were involved (highlighted in red in Fig. 6), particularly the rate coefficients governing autoxidation propagation and $NO_3-RO_2^{\cdot}$ termination reactions. To address these, rate coefficients identical to those used in the BCARY + O_3 system were adopted, under the assumption that the oxidation kinetics and radical behavior of BCARY were sufficiently similar between the two mechanisms. Notably, the only parameter specifically constrained for this mechanism was the branching ratio η of the reaction R_{n0}, which was determined by fitting to the SOA volume concentrations observed in Case 5.[6] The $RO_2^{\cdot}$ molecules (BCALAO2 and $C_{15}H_{24}ONO_3O_2^{\cdot}$) undergoing autoxidation are not exactly the same but share similar structural features. They have the same number of carbons and a similar number of hydrogens and functional groups. The main difference between the two $RO_2^{\cdot}$ radicals is that one has an aldehyde and the other a nitrate group. While this implies their H-shift kinetic parameters are not identical, they are likely of the same order of magnitude.

2.4 Configuration of simulations

2.4.1 SSH-aerosol model setup overview. Simulations using the mMCM and the developed autoX-MCM were performed under the conditions corresponding to the different selected laboratory experiments. These simulations were conducted using the SSH-aerosol model v2.0.[26,27]

The SSH-aerosol model is a 0-D box model designed to represent the formation and evolution of secondary aerosols with varying levels of complexity. This modular model resolves aerosol dynamics with the SCRAM (Size-Composition Resolved Aerosol Model) module,[31] which includes coagulation, condensation/evaporation, nucleation, and particle mixing states by classifying particles based on both composition and size. The partitioning of the organic compounds is computed based on the saturation vapor pressure (P_{sat}) of compounds with the thermodynamic model SOAP (Secondary Organic Aerosol Processor),[32] which accounts for non-ideality (absorption by the aqueous phase of particles, interactions between organic compounds and with inorganic compounds) based on the molecular composition of the aerosol.

The SSH-aerosol model can simulate gas-particle partitioning using either a thermodynamic equilibrium approach or a dynamic approach. The equilibrium approach assumes instantaneous phase equilibrium between gas and particle phases, which offers computational efficiency but may oversimplify mass transfer processes, particularly for larger

particles. In contrast, the dynamic approach explicitly simulates the kinetic mass transfer between phases, providing a more accurate representation. The dynamic approach was used in the current study to represent accurately SOA formation and the competition between condensation/evaporation and nucleation which was considered for ELVOCs.

Thermodynamic properties such as P_{sat} and enthalpy of vaporization (ΔH_{vap}) govern the volatility of oxidation products and thus determine their partitioning behavior between the gas and particle phases. These properties were calculated with structure–activity–relationship (SAR) methods. Thermodynamic properties were calculated using UManSysProp[33] with eight different estimation methods, including:

- EVAPORATION ('evap')[34]
- SIMPOL ('sim')[35]
- Six hybrid methods combining two vapor pressure estimation methods ('v0'[36] and 'v1'[37]), with three boiling point estimation methods('b0',[38] 'b1',[39] and 'b2'[40]).By default, the 'v0b0' method was used.

To accurately reproduce the BCARY oxidation in the absence of seeds, new particle formation is simulated using the organic nucleation module embedded in SSH-Aerosol as nucleation may have a critical role in early SOA formation. The nucleation rate J_{nucl} (particles cm^{-3} s^{-1}) is parameterized as:

$$J_{nucl} = k_{nucl}\,[\text{organics}]^{\alpha} \tag{1}$$

Here, k_{nucl} is an empirical parameter optimized by fitting model-predicted number concentrations to experimental data. α was set to 2 as the default in this study. Compounds included in the nucleation scheme are filtered by a vapor pressure threshold (ELVOCs) to ensure only sufficiently low-volatility species are considered. [Organics] (µg m^{-3}) is the concentration of the nucleating organic species.

The formation of new particles is a fundamental process in SOA formation and is known to be highly sensitive to ambient temperature. The new particle formation rate J_{nucl} was calculated with eqn (1).[41] To ensure the model could accurately simulate particle dynamics across different environmental conditions, the nucleation rate coefficient (k_{nucl}, particles µg^{-2} m^3 s^{-1}) was treated as the key tunable parameter. For this purpose, the experimental particle number concentration measurements from Gao et al.[6] for three distinct temperatures (273 K, 298 K, and 313 K) were used to constrain the values of k_{nucl} at the different temperatures.

2.4.2 Simulation-specific settings. Building upon the general SSH-Aerosol configuration described in Section 2.4.1, this subsection outlines the specific model parameters and settings applied in the reproduction of experiments by Gao et al.,[6] Jokinen et al.,[14] Richters et al.[16]

For flow-tube experiments, the objective was to directly compare modeled ELVOC yields with those derived from CI-APi-TOF measurements.[14,16] Due to the short timescale of these experiments (a few seconds), which is insufficient to initialize new particle formation, only gas-phase chemistry was considered in the model simulation.

For the chamber simulations of Gao et al.,[6] particle dynamics were explicitly resolved to capture the evolution of size-resolved SOA formation. The model was configured with 50 logarithmically spaced size bins covering the diameter range from 1 nm to 1 μm. The ELVOC nucleation module was activated to simulate new particle formation. The calculated particle size distributions were integrated over the range 13.6–792 nm to match the detection range of the SMPS used in the experiments.

Wall losses were also considered in the simulation for the experiments of Gao et al.[6] Here, the particle wall loss rate constant was set to 2.008×10^{-5} s^{-1} in order to reproduce the decay of SOA concentrations observed after the conclusion of Case 5 (experiment time up to 230 min), specifically during a post-experiment period (238–988 min) when SOA production had largely ceased, approximately one hour after the last BCARY injection. The reversible wall losses of gases were also considered using the wall loss module described by Sartelet et al.[27] The wall loss rate of gases was calculated by using an eddy diffusion coefficient equal to 0.2 s^{-1} which led to a wall loss rate varying for semivolatile species between 1.0×10^{-4}–6.0×10^{-4} s^{-1} corresponding to the range reported by Saathoff et al.[42] for the chamber used by Gao et al.[6]

2.5 Simulation evaluation

To ensure a consistent and meaningful comparison between simulations and experiments, two primary metrics were derived from the model outputs, ELVOC (or ELVOC$^+$) molar yield (defined as the ratio between the amount of ELVOC or ELVOC$^+$ produced and the amount of BCARY that has reacted) and SOA volume concentration.

To minimize uncertainties associated with selecting a particle density to derive a SOA mass loading from SMPS data, model—measurement comparisons were conducted using calculated SOA volume concentrations rather than mass concentrations. In the chamber study conducted by Gao et al.,[6] mass concentrations were derived from SMPS data based on a determined average density (1.09 ± 0.12 g cm^{-3}). However, this density was assumed constant during the experiment, although it probably changes during the experiment with SOA composition.

The mass concentrations simulated with SSH-aerosol were converted to volume concentrations by dividing by the particle density, which was estimated from the density of the different compounds. The density of each condensable product was determined from its elemental composition, using the parameterization from Kuwata et al.[43] based on H : C and O : C ratios. To account for nitrogen-containing species, the formula was modified to include nitrogen in the same manner as oxygen. The resulting equation for organic aerosol density (ρ_{org}) in g cm^{-3} is:

$$\rho_{org} = \frac{12 + H/C + 16 \times (O+N)/C}{7 + 5 \times H/C + 4.15 \times (O+N)/C} \text{g cm}^{-3}$$

where C, H, O, and N denote the number of carbon, hydrogen, oxygen, and nitrogen atoms, respectively. This composition-based approach enables more consistent and accurate comparisons between model simulations and experiments.

$$C_{SOA,volume} = \sum_{i=1}^{n} \frac{C_{i,mass}}{\rho_i}$$

where $C_{SOA,volume}$ is the total SOA volume concentration (nL m^{-3}), $C_{i,mass}$ is the mass concentration of component i (μg m^{-3}), and ρ_i (g cm^{-3}) is the density of component i.

2.6 Sensitivity tests

To assess the model's response to key uncertain parameters in SOA formation, a set of sensitivity analyses was conducted in order to identify the most influential factors.

Three types of sensitivity tests were conducted:

• Sensitivity tests on saturation vapor pressure estimations: In these tests, SOA concentrations were computed with the different P_{sat} methods available in UManSysProp ('evap', 'sim', 'v0b0', 'v0b1', 'v0b2', 'v1b0', 'v1b1', and 'v1b2') in order to analyze the effect of uncertainties on P_{sat} on simulation results.

• Sensitivity tests on key kinetic parameters for autoxidation: AutoX-MCM relies on the estimation of some kinetic parameters based on a fitting approach to experimental results from different studies. This sensitivity analysis was conducted to determine the influence of each parameter and the robustness of the mechanism.

• Sensitivity tests on oligomerization: Oligomerization can strongly affect SOA composition and formation. In order to investigate the influence of this process, the bulk oligomerization parameterization of Couvidat et al.[44] was used. In this parameterization, oligomerization is represented via a 2nd order chemical reversible reaction, which is unfavored by humid conditions. All particle-phase organic compounds are assumed to undergo oligomerization.

3 Results

3.1 Parameters optimization

As described in Section 2.3, the optimization procedure aims to estimate the key reaction parameters related to ELVOC formation pathways within autoX-MCM, by minimizing the differences between the model and measurements. The constrained parameters' values are shown in Table S1.

As shown in Table 3, the base mechanism mMCM, despite containing 13 ELVOC species, fails to reproduce ELVOC (and ELVOC$^+$) yields across all three experimental cases and could not simulate SOA formation. In contrast, the incorporation of

autoxidation-driven ELVOC formation in autoX-MCM markedly improved model performance. The optimized mechanism simulated yields close to the experimental data. For instance, in Case 1,14 an ELVOC yield of 1.17% was simulated with autoX-MCM, well within the experimental uncertainty range $(1.70^{+1.28}_{-1.28}\%)$ reported by Jokinen et al.[14] Similarly, results from Cases 2 and 3 show that simulated yields with autoX-MCM (0.46% and 1.36%, respectively) consistent with the experimental ranges $(0.37^{+0.5}_{-0.3}\%$ and $1.37^{+1.8}_{-0.9}\%$, respectively) reported by Richters et al.[16] Furthermore, in Case 4,6 the volume SOA concentration was accurately reproduced with autoX-MCM the volume SOA concentration in the 1st stage of the experiment (6.48 vs. 6.47 nL m^{-3}), showing that the inclusion of the autoxidation pathway is essential to accurately simulate SOA formation from BCARY ozonolysis.

To reduce overfitting and ensure independent validation, only the Stage 1 experiment at 298 K was used to constrain key parameters in autoX-MCM, while the remaining experiments (including 273 K and 313 K cases) were used exclusively for validation. Only short-scale experiments without seeds are used to fit the parameters relevant to ELVOC formation.

3.2 Nucleation rate as a function of temperature

For each temperature and each chemical mechanism (mMCM and autoX-MCM), the nucleation rate coefficient k_{nucl} was individually fitted to reproduce the measured peak particle number concentration. For the reference case at 298 K (Case 5), this approach yields values for k_{nucl} of 3.50×10^{-7} and 1.53×10^{-7} particles μg^{-2} m^3 s^{-1} for the autoX-MCM and mMCM mechanisms, respectively. As shown in Fig. 1b, using these coefficients allowed the model to capture both the initial peak and the subsequent decay of the particle number concentration. However, a minor discrepancy in the timing of the number concentration peak is observed at 298 K: the autoX-MCM mechanism simulated the peak a few minutes earlier, whereas

Table 4 Fitted nucleation rate coefficients (k_{nucl}, in particles μg^{-2} m^3 s^{-1}) for Case 5–7 derived using the 'v0b0' P_{sat} methods for the autoX-MCM and mMCM mechanisms. For comparison, values calculated from the empirical temperature dependence formula (eqn (2)) are listed in the final column

Case	T (K)	autoX-MCM	mMCM	Eq$_k$
5	298	3.59×10^{-7}	1.56×10^{-7}	3.59×10^{-7}
6	273	2.97×10^{-6}	8.87×10^{-7}	2.97×10^{-6}
7	313	1.70×10^{-7}	1.05×10^{-7}	1.01×10^{-7}

the mMCM mechanism simulated it slightly later than the experiments. This suggests that while the overall production potential of nucleating species is well represented, the timing of their initial appearance may differ between mechanisms, potentially influenced by both formation rates and ELVOC concentrations. This fitting procedure was then repeated for the low-temperature (273 K, Case 6) and high-temperature (313 K, Case 7) experiments, where this timing mismatch shows a different temperature-dependent behavior. The complete set of optimized nucleation coefficients is presented in Table 4.

As expected, the results reveal a clear temperature dependence for k_{nucl}, with its value being highest at 273 K and decreasing at higher temperatures. This decrease with temperature is consistent with the temperature dependence of the overall nucleation rate reported in previous literature.[45] Based on the estimations of the nucleation rate coefficients with the autoX-MCM mechanism at the different temperatures, the following empirical parameterization was derived to estimate the evolution of coefficient k_{nucl} with temperature:

$$k_{nucl}(T) = k_{nucl}(298 \text{ K})\exp\left(-\frac{T - 298}{11.83}\right) \qquad (2)$$

This equation describes an exponential decrease in the overall nucleation rate parameter k_{nucl} (in particles μg^{-2} m^3 s^{-1})
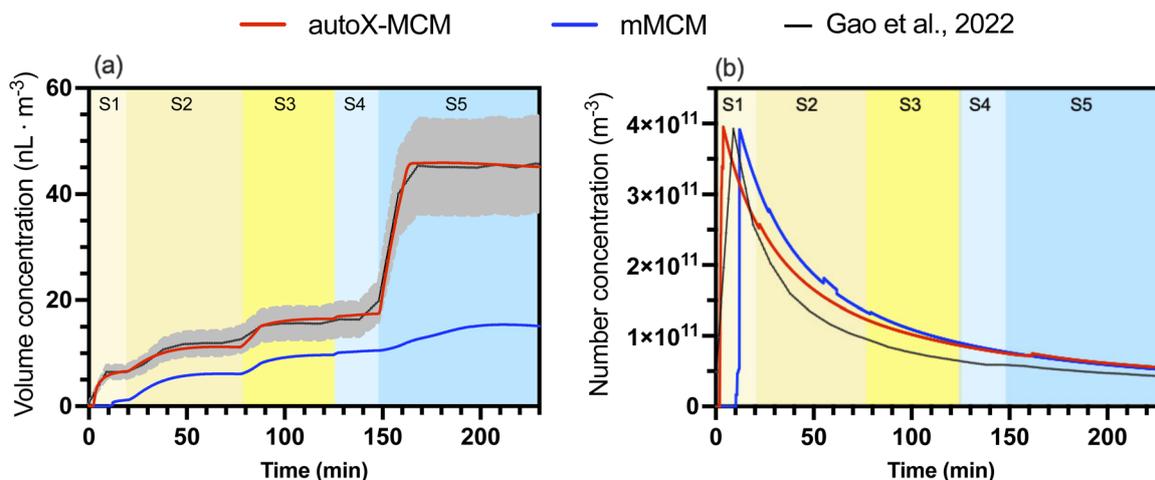

Fig. 1 Model-measurement comparison for Case 5 (BCARY oxidation at 298 K, RH = 27%): (a) SOA volume concentration (nL m^{-3}); (b) particle number concentration (m^{-3}). The black lines (with gray error bars) represent chamber measurements reported by Gao et al.[6] The solid blue and red lines correspond to the averaged simulated concentrations simulated with mMCM and autoX-MCM mechanisms, respectively. The shaded area corresponds to the uncertainties of measurements. The different stages of the experiments are illustrated by different background colors ranging from yellow (pre-NO$_2$ injection) to blue (post-NO$_2$ injection).

with increasing temperature. The fitted k_{nucl} values for the autoX-MCM at 298 K and 313 K are in good quantitative agreement with the values estimated by the empirical formula.

To ensure the highest fidelity for each specific experimental case, the individually fitted k_{nucl} values were used for all subsequent simulations presented in this study. Nevertheless, the k_{nucl} values from the empirical formula (eqn (2)) could be used in other studies to represent nucleation as a function of temperature.

3.3 AutoX-MCM performances

To further evaluate the performance of autoX-MCM, the improved mechanism was compared with SOA volume concentrations against experimental data from Cases 5–7 as detailed in Table 2. The analysis was performed in 3 steps:

- Comparison of SOA volume concentrations at 298 K focusing on the stages before NO_2 injection in order to evaluate SOA formation from BCARY + O_3 at 298 K.

- Comparison of SOA volume concentrations at the different temperatures focusing on the stages before NO_2 injection.

- Comparison of SOA volume concentrations at the different temperatures focusing on the stages after NO_2 injection for which SOA should mostly come from the BCARY + $NO_3^•$ reaction.

3.3.1 BCARY + O_3 mechanism. Fig. 1a shows the evolution of simulated SOA volume concentrations compared to the SMPS measurements from Gao *et al.*[6] at 298 K.

Simulations using mMCM significantly underestimated SOA formation. In contrast, the autoX-MCM mechanism accurately captured both the trend and magnitude of the measured SOA volume concentration, particularly at the beginning of the experiment. The experimental data show a rapid initial increase in particle growth, followed by a more gradual increase leading to a total increase of 6.47 nL m^{-3} during the 1st stage (against 6.47 nL m^{-3} for observations), which is missing in the mMCM

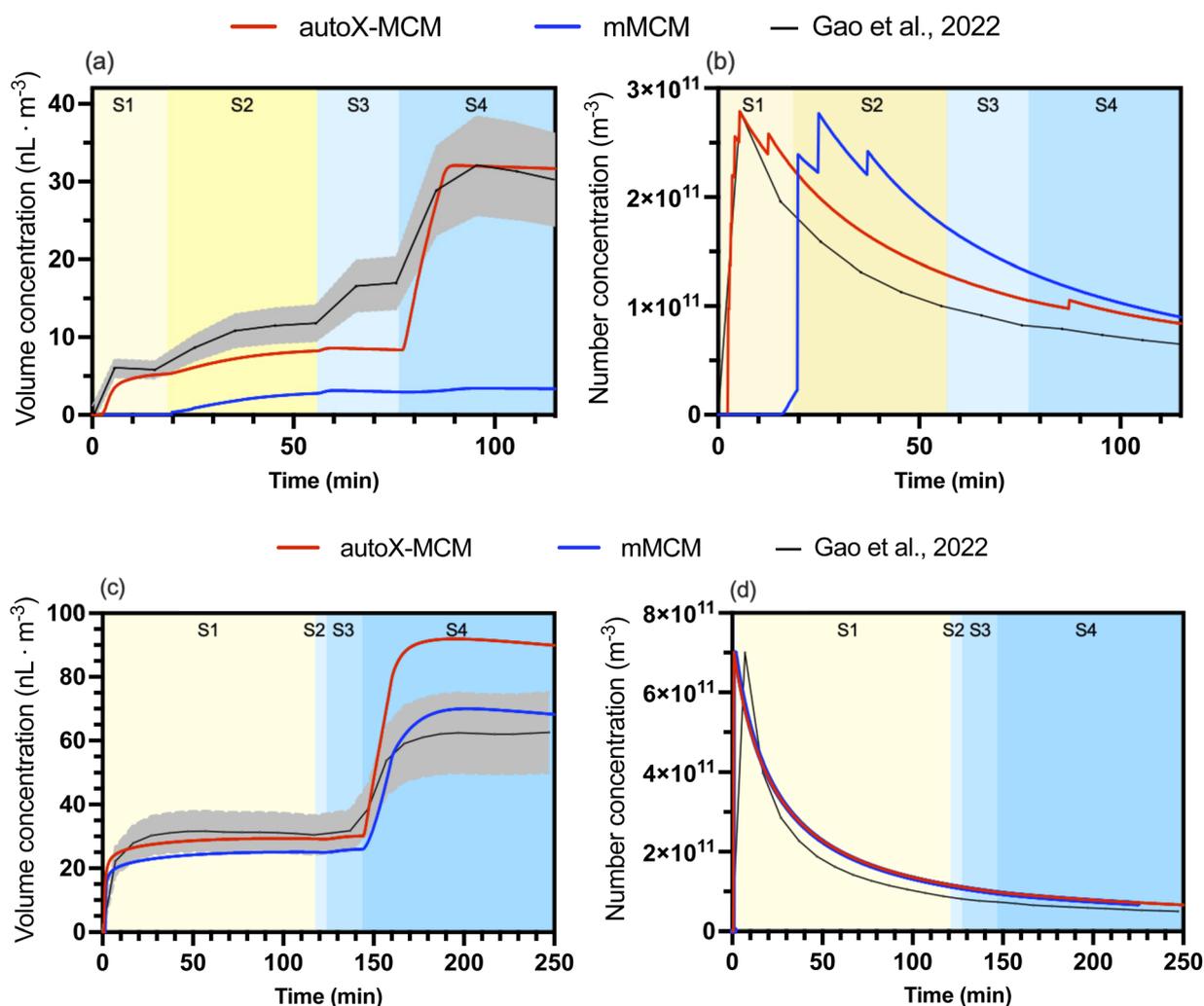Fig. 2 Model-measurement comparison at 313 K (upper panels) and at 273 K (lower panels): (a) and (c) SOA volume concentration (nL m^{-3}); (b) and (d) particle number concentration (m^{-3}). The black lines (with gray error bars) show the chamber measurements. The solid blue and red lines correspond to the averaged simulated concentrations simulated with mMCM and autoX-MCM, respectively. The shaded area corresponds to the uncertainties of measurements. The different stages of the experiments are illustrated by different background colors ranging from yellow (pre-NO_2 injection) to blue (post-NO_2 injection).

simulation but well reproduced with the implementation of the ELVOC formation process.

After injecting abundant O_3 into the system, SOA concentrations during the 2nd stage increased by 4.56 nL m^{-3} in the model, compared to 6.13 nL m^{-3} for observations. Following the introduction of additional BCARY, simulated SOA increased during the 3rd stage by 5.37 nL m^{-3} (against 3.40 nL m^{-3} for observations).

To further assess the robustness and predictive capability of the autoX-MCM, it was evaluated at different temperatures. Temperature affects multiple aspects of SOA formation and evolution (including gas-particle partitioning, chemical reactions, and nucleation), which are represented in the model. Additional comparisons were therefore conducted for the experimental studies of Gao *et al.*[6] at 273 K and 313 K, respectively. SOA volume concentrations simulated under these conditions are shown in Fig. 2.

At 313 K, the SOA concentrations were well simulated during the 1st stage using autoX-MCM but underestimated using mMCM. The measured number concentration peak reached 2.78×10^{11} m^{-3} at 330 s against a simulated peak at 320 s with a concentration of 2.79×10^{11} m^{-3} for autoX-MCM. In contrast, the modeling of the peak is extremely delayed using mMCM (at 1500 s) due to the lack of ELVOC formation. However, autoX-MCM underestimated the increase of volume concentrations reported by Gao *et al.*[6] during stage 2 (corresponding to the injection of additional O_3 in the chamber), with a mean error bias of −3.13 nL m^{-3}.

At 273 K, the 1st stage (pre-NO$_2$) of the experiment was well represented using both the mMCM and the autoX-MCM mechanisms, as the simulated concentrations are within the uncertainties of measurements. However, the autoX-MCM mechanism shows substantially better results, with a small negative bias of only −1.20 nL m^{-3} (−3.9%), compared to a bias of −5.40 nL m^{-3} (−17.7%) for mMCM.

3.3.2 BCARY + NO$_3^•$ mechanism. This section presents the performance of the autoX-MCM mechanism in simulating SOA and particle number concentrations due to BCARY oxidation by NO$_3^•$ during the last stage of Cases 5–7 across three temperatures (273 K, 298 K, and 313 K).

The measured and simulated SOA formation by BCARY + NO$_3^•$ at the different temperatures is illustrated by the last stage of each experiment in Fig. 1 and 2.

At 298 K (Fig. 1), the autoX-MCM model reproduced both the temporal evolution and magnitude of SOA volume concentration after NO$_2$ injection, simulating 43.61 nL m^{-3} at 228 min compared with the measured value of 42.77 nL m^{-3}. While the mMCM simulation underestimated SOA formation (15.20 nL m^{-3} at 228 min), the simulation with autoX-MCM captured the rapid increase in SOA following NO$_2$ (stage 4) and BCARY (stage 5) injection. This improvement was attributed to the inclusion of highly oxygenated products *via* autoxidation pathways in the BCARY + NO$_3^•$ mechanism.

The autoX-MCM mechanism also performed well at 313 K (Fig. 2, upper panels) as the autoX-MCM significantly improves SOA concentrations during the last stage, increasing the simulated SOA volume concentration at 115 min from 3.37 nL m^{-3}

with mMCM to 31.67 nL m^{-3} with autoX-MCM. This revised result aligns almost perfectly with the measured concentration of 30.18 nL m^{-3}. However, while the final concentrations are well reproduced, the model seems to compensate for a lack of SOA formed during stages 2 and 3, with a mean error bias of −7.18 nL m^{-3} after the injection of NO$_2$ (stage 3). It could indicate an overestimation of SOA by BCARY + NO$_3^•$ as the simulated increase of concentration during stage 4 was around 23 nL m^{-3} for autoX-MCM against 13 nL m^{-3} for observations.

At 273 K (Fig. 2, lower panels), both mechanisms tend to overestimate SOA formation during the post-NO$_2$ condition, with autoX-MCM resulting in the largest overestimation (around 46 ± 20%). The simulated SOA concentrations with mMCM were higher than observed, and inclusion of autoxidation pathways further amplified this bias. This discrepancy may stem from an overestimation of reaction rates under cold conditions or missing processes not accounted for in the model. Alternatively, temperature-dependent processes such as wall losses, volatility, condensation dynamics, or heterogeneous chemistry may not be adequately represented in the current model, leading to excessive SOA accumulation at low temperatures.

Beyond total SOA loading, the autoX-MCM also significantly improves the simulation of the organic nitrate (org-N) mass fraction within the total organic aerosol, as summarized in Table S3. For instance, at 298 K (Case 5b), an org-N mass fraction simulated with autoX-MCM was 62.00%, which is in good agreement with the measured value of 58.96% from Gao *et al.*[6] This contrasts sharply with the substantial underestimation by the mMCM (28.50%). Similarly, at 313 K (Case 7b), the simulation with autoX-MCM of 70.30% was much closer to observations 61.06% than the mMCM results (21.37%), a trend consistently observed for Case 6b (273 K) as well. For both 313 K and 273 K, the difference between the autoX-MCM simulation and the measurement falls within the experimental error tolerance reported by Gao *et al.*[6] (±20%). These results indicate that the inclusion of autoxidation pathways, particularly those involving NO$_2$, leads to a more accurate representation of the molecular composition of the SOA, especially regarding the contribution of the nitrate functional group.

Furthermore, the modeled composition of organic nitrates was analyzed and compared with the experimental data from Gao *et al.*[6] For consistency, the molar fraction of each org-N species. Both experiment and simulation show that C_{12-15} compounds, corresponding to all monomeric org-N species represented in the mechanisms, dominate the total organic nitrate molar fraction (approximately 77% across all tested temperatures in the simulation *versus* 69.6% in the experiment). Low-carbon nitrates (C_{2-11}) contribute nearly 0% in the simulation compared to about 8% in the experiment, while larger org-N (C_{16-46}) account for about 22% in the simulation, a proportion nearly identical to that observed experimentally. The model underestimates the contribution of low-carbon org-N species (suggesting an underestimation of fragmentation processes or of the partitioning of low-carbon organic nitrates toward the particle phase) and overestimates the contribution of C_{12-15} org-N species, though still within the 20%

experimental uncertainty. This difference primarily arises from model design: the autoX-MCM mechanism explicitly parameterizes autoxidation only for ELVOCs and total SOA mass yield, whereas smaller org-Ns formation is only represented in the base MCMv3.3.1 mechanism. Thus, the discrepancy likely reflects uncertainties in these fragmentation processes rather than limitations of the new autoxidation parameterization itself.

To further investigate the chemical characteristics underlying these compositional trends, the elemental ratios (O C and N C) and the average numbers of O and N atoms were compared across the same three carbon-number ranges defined above. For the monomeric org-N (C_{12-15}), both O C and the average O numbers are lower by about two oxygen atoms compared to the experiment, implying that the overall oxidation degree in both mMCM and autoX-MCM may be slightly underestimated. In contrast, the simulated N C ratios and nitrogen content agree well with observations, indicating a globally correct nitrate incorporation in autoX-MCM. For the species C_{16-46}, the model reproduces the experimental O C well (around 0.37), confirming that the oxidation state is realistically captured by autoX-MCM mechanism. However, the higher average O number (11 *vs.* 9 in the experiment) and slightly lower N C suggest that the modeled C_{16-46} have somewhat longer carbon skeletons (*e.g.*, C_{30} rather than C_{25}). This indicates that the parameterized autoxidation scheme may overestimate molecular size while preserving realistic oxidation levels.

Overall, the autoX-MCM mechanism captures the oxidation pattern of nitrate-containing SOA well, though the dimer representation could be refined toward slightly smaller skeletons.

3.4 Sensitivity analysis

3.4.1 Saturation vapor pressure estimation methods. To evaluate the impact of different P_{sat} estimation methods on SOA formation, each method was applied to both the base mMCM

mechanism and the developed autoX-MCM mechanism. The simulated SOA volume concentrations with the different estimation methods were then compared against chamber observations from Gao *et al.*,[6] shown as the dotted black line and shaded uncertainty range in Fig. 3. The root mean square error (RMSE) was used as the performance metric.

Before evaluating the SOA formation, it was first crucial to ensure that each simulation accurately reproduced the new particle formation. The nucleation process is driven by the species with the ELVOCs, and the number of compounds meeting this criterion is highly dependent on the chosen P_{sat} method. Therefore, to meet the experimental number concentration well for each scenario, the nucleation rate was individually fitted for each combination of chemical mechanism and P_{sat} method to match the peak number concentration observed in the experiment of Case 5. The resulting fitted nucleation rates, detailed in Table S2, were found to be highly sensitive to the choice of P_{sat} method. This sensitivity is directly linked to the number of species classified as ELVOCs. For instance, methods such as 'evap', 'v0b0', and 'v1b2' classify several important species (such as $C_{15}H_{24}O_8$ from the autoxidation in BCARY ozonolysis) as ELVOCs, while some other methods seem to miss major compounds as ELVOC. With the 'v1b0' method, the pool of nucleating species is severely limited as the only considered ELVOC is generated during the last stage after NO_2 injection. Therefore, it is not possible to determine a nucleation rate parameter for this method. For the sake of the exercise, a value of 1.65×10^{-7} particles μg^{-2} m^3 s^{-1} is used for 'v1b0'.

Having normalized the new particle formation by individually fitting the nucleation rate of each condition, the performance of each P_{sat} method and chemical mechanism in simulating SOA formation was then evaluated. The results, shown in Fig. 3, reveal distinct differences in the performance of the mMCM and autoX-MCM.

As illustrated in Fig. 3b, with the mMCM mechanism, only the 'sim' method seems to reproduce the SOA formation during the 1st stage of the experiment (where the RMSE is 1.51 nL m^{-3},
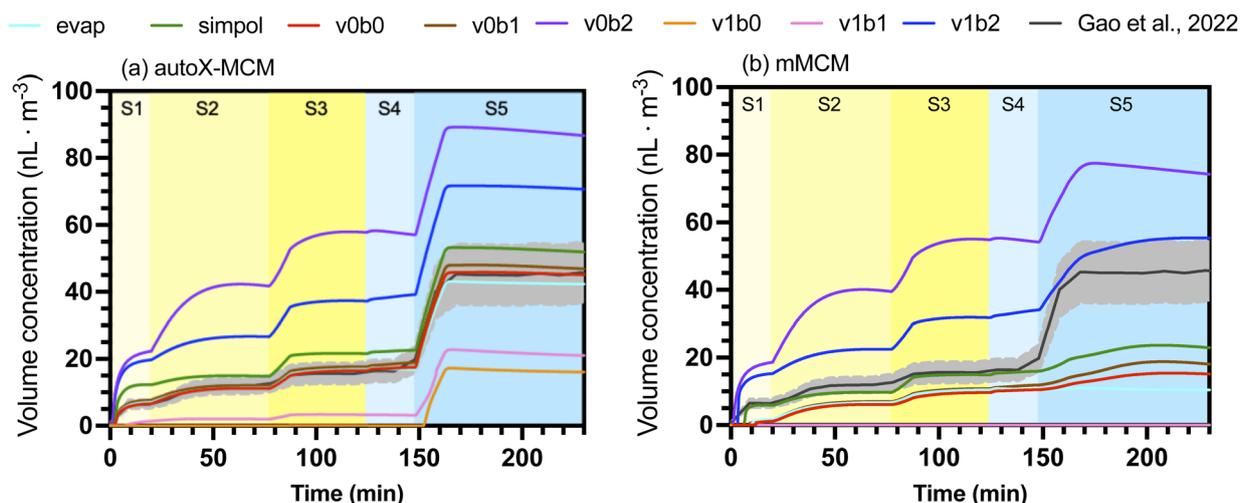

Fig. 3 Time series of simulated SOA volume concentrations using eight different P_{sat} computation methods using (a) autoX–MCM and (b) mMCM. The black dotted line and shaded area represented the observed SOA concentration and uncertainty reported from Gao *et al.*[6]

Table 5 Root mean square error (RMSE, nL m^{-3}) between simulated and observed SOA concentrations for different P_{sat} estimation methods, using autoX-MCM and mMCM mechanisms. "S1" refers to the experimental 1st injection

P_{sat} estimation method	S1	All stages	mMCM S1	All stages
Evap	0.65	1.50	4.43	19.80
sim	5.2	6.18	1.51	12.76
v0b0	0.53	0.88	4.81	17.93
v0b1	1.09	2.05	4.44	16.14
v0b2	13.28	36.99	10.15	30.74
v1b0	4.59	19.46	5.27	27.59
v1b1	5.24	15.78	5.27	27.59
v1b2	11.37	21.06	7.35	11.63

far lower than the other methods). Other methods either significantly overestimated ('v1b2' and 'v0b2') or significantly underestimated volume SOA concentrations. Moreover, even if mMCM using 'sim' seems to provide good results at the end of the 1st stage, it failed to reproduce the rapid SOA growth in the first minutes of the experiment, as simulated SOA began to increase significantly after 6.5 min.

In contrast, as shown in Fig. 3a, simulations using the autoX-MCM exhibit a marked improvement: most P_{sat} estimation methods (except 'v1b0' and 'v1b1') reproduced a rapid SOA growth during the early stage of the experiment. Moreover, several P_{sat} estimation methods ('evap', 'v0b0', and 'v0b1'), closely aligned with the measured trend throughout the experiments. However, simulation results with the autoX-MCM mechanism span a four-fold range in SOA volume concentration depending on the P_{sat} method used. This sensitivity test indicates that the accuracy of the mechanism is highly sensitive to the choice of volatility estimation method.

To quantitatively assess the model—observation agreement, the RMSE was calculated between simulated and measured SOA volume concentrations under each P_{sat} method (Table 5). For autoX-MCM, methods such as 'v0b0' and 'evap' achieved the

lowest RMSE values across all stages, indicating better performance in reproducing the SOA time series. In contrast: most of the tests using the mMCM yield significantly higher RMSE, quantitatively confirming the failure to capture the SOA formation process accurately. Using autoX-MCM, a cluster of methods, including 'evap', 'v0b0', and 'v0b1', demonstrated the best performance, suggesting they provide the most realistic P_{sat} estimations. 'v0b2' and 'v1b2' appear to significantly underestimated volatility, leading to excessive partitioning and an overprediction of SOA loading. On the contrary, 'v1b0' and 'v1b1' seem to estimate unrealistically high P_{sat} leading to almost no SOA formation throughout the experiment.

Among the tested methods, the default P_{sat} estimation method 'v0b0' was shown to provide the best results with the lowest RMSE.

3.4.2 Influence of key parameters for autoxidation. To investigate the influence of specific autoxidation reactions on the formation of ELVOCs and SOA, a systematic sensitivity analysis was performed by perturbing the rate constants and stoichiometric ratios of key reactions of the autoxidation mechanism. An ensemble of model sensitivity tests, detailed in Table 6, was constructed based on the optimized mechanism (hereafter referred to as 'optimized autoX-MCM'). Each scenario involved a modification of a specific set of parameters categorized into three groups: stoichiometric coefficient scaling, global rate scaling, and specific reaction scaling. Fig. 4a illustrates the sensitivity of SOA formation to different parameters involved in the autoxidation mechanism from BCARY ozonolysis.

The test was first performed in the chamber conditions of Case 5. Unsurprisingly, the model exhibited the highest sensitivity to the stoichiometric yield of the initial RO$_2^•$ (BCALAO2) starting the autoxidation propagation ('ky' scenarios). Doubling this yield ('kyx2') resulted in a significant increase of the 1st stage SOA volume concentration (11.36 nL m^{-3} at 19 min), exceeding the experimental value (6.46 nL m^{-3}) by more than 75.8%. Conversely, the model was found to be relatively

Table 6 List of key parameters changed in the different sensitivity tests

| Sensitivity tests	Description
stoichiometric coefficient scaling	
kyx0.5	Yield of BCALAO2 in reaction R_{n1} multiplied by 0.5
kyx2	Yield of BCALAO2 in reaction R_{n1} multiplied by 2
Global rate scaling	
hshift_all3	Decreasing H-shift reaction rate of BCARY + O$_3$ scheme (reactions R_1) to minimal value
hshift_all20	Increasing H-shift reaction rate of BCARY + O$_3$ scheme to maximal value
rt_allmin	Decreasing all RO$_2^•$ + RO$_2^•$ termination rates of BCARY + O$_3$ autoxidation reactions R_4 to minimal value
rt_allmax	Increasing all RO$_2^•$ + RO$_2^•$ termination rates of BCARY + O$_3$ autoxidation reactions R_4 to maximal value
allx0.5	All fitted kinetics of BCARY + O$_3$ autoxidation reaction multiplied by 0.5
allx2	All fitted kinetics of BCARY + O$_3$ autoxidation reaction multiplied by 2
N_allx0.5	All fitted kinetics of BCARY + NO$_3^•$ autoxidation reaction multiplied by 0.5
N_allx2	All fitted kinetics of BCARY + NO$_3^•$ autoxidation reaction multiplied by 2
Specific reaction scaling	
Nkyx0.5	Rate of BCARY + NO$_3^•$ reaction multiplied by 0.5
Nkyx2	Rate of BCARY + NO$_3^•$ reaction multiplied by 2
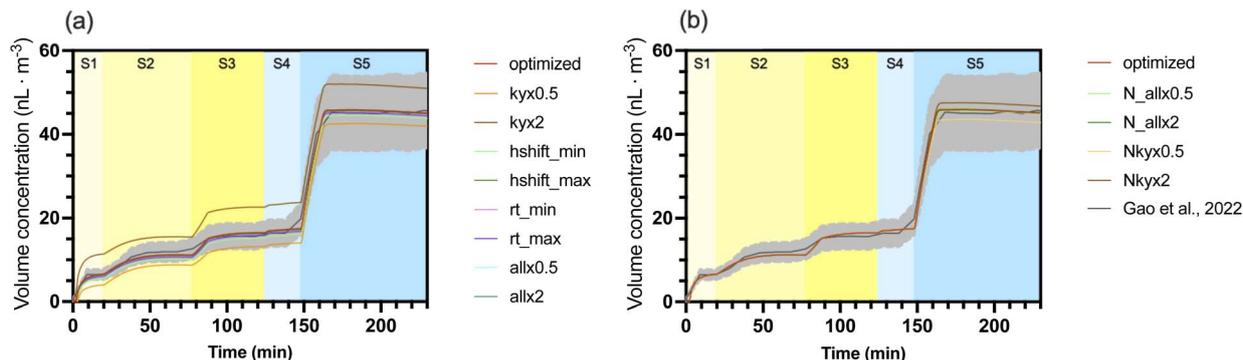
Fig. 4 Model-measurement comparison for Case 5 (BCARY ozonolysis at 298 K, RH = 27%) simulated with different scenarios ((a) $NO_3^{\bullet}$-initiated BCARY reactions (b) -initiated BCARY reactions) of autoX-MCM. The measurements of the chamber were shown in a dotted black line. The grey shadow area indicates the uncertainties of measurements.

insensitive to a global scaling of all autoxidation kinetics ('all' scenarios): increasing or decreasing the kinetics by a factor of 2 changed the mean bias (MB) by only -0.05–0.02 nL m^{-3} compared with the optimized simulation. The rates of the H-shift propagation steps ('hshift' scenarios) and $RO_2^{\bullet} + RO_2^{\bullet}$ termination rates ('rt' scenarios) showed a moderate influence on the final SOA mass. Even maximizing the termination rates ('rt_max') or minimizing the H-shift rates ('hshift_min') caused minor deviations of 0.66 nL m^{-3} and 1.31 nL m^{-3}, respectively. The corresponding opposite tests ('rt_min' and 'hshift_max') resulted in deviations of less than 0.2 nL m^{-3}.

A similar analysis for Case 5 was conducted for the parameters of the -initiated autoxidation mechanism (Fig. 4b). These results indicate a strong model sensitivity to the initial reaction rate between BCARY and $NO_3^{\bullet}$ ('Nky' scenarios). Halving this specific rate ('Nkyx0.5') led to a noticeable decrease of both particle volume (by 2.04 nL m^{-3}). In contrast, a global scaling of all subsequent autoxidation steps ('N_all' scenarios) had a less pronounced effect on the simulation outcome, with a larger deviation reaching -0.17 nL m^{-3} ('N_all' scenario). The importance of the rate of the BCARY + $NO_3^{\bullet}$ is probably due to the competition between O_3 and $NO_3^{\bullet}$. Increasing the rate increases the amount of BCARY reacting with $NO_3^{\bullet}$. As the simulation of $NO_3^{\bullet}$ concentrations is probably uncertain, the sensitivity to this parameter could also be interpreted as the effect of uncertainties on $NO_3^{\bullet}$ simulation.

The simulations for flow-tube experiments were found to be very sensitive to parameters, with the mean normalized bias (MNB) across the sensitivity tests reaching 58.7%. This is probably due to the short time residency of the flow-tube experiments. For the experiments with the lowest time residency (7.9 s for Cases 2 and 3 from Richters et al.[16] illustrated in Fig. 5b and c), ELVOC concentrations were also highly sensitive to the $RO_2^{\bullet}$ termination rates ('rt' scenarios). Increasing these rates consistently increases ELVOC yields (with the effect being particularly pronounced under Case 2) by more than a factor of 3. Conversely, using the minimal $RO_2^{\bullet}$ termination rate ('rt_min') led to divergent responses: in Case 2, the yield was slightly increased by 12%, while in Case 3 it was clearly decreased by 45%. The sensitivity to these reactions is high because the model needs to ensure that radicals are transformed into stable compounds within the duration of the experiment. However, the influence of these termination reactions rapidly reduced with time. For the experiments of Jokinen et al.[14] (20 s flow-tube experiments), its impact had become less pronounced, with an MNB of about 44% across the eight scenarios.

For the chamber simulation with longer residence time, the system becomes almost entirely insensitive to parameter changes (most of the concentration changes were lower than 2.0 nL m^{-3}), with the largest deviation (in 'kyx2' scenario) being only a 13% increase of the final SOA volume concentration. The autoxidation can therefore be considered as robust, especially
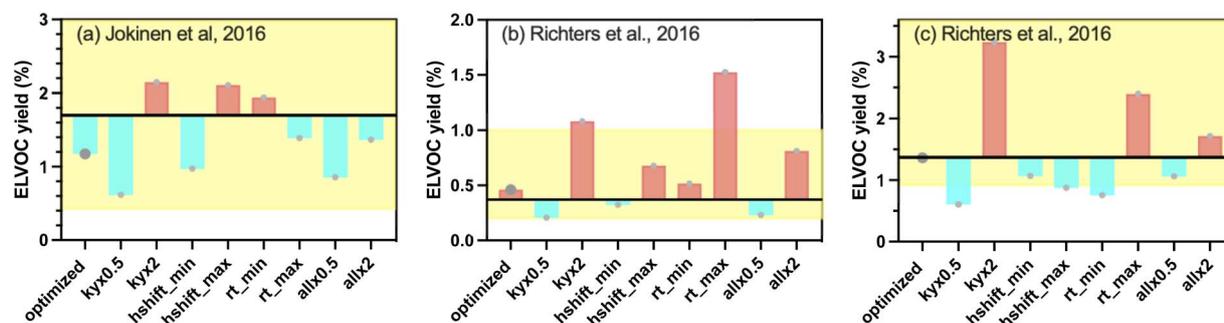

Fig. 5 Model-measurement comparison for (a) Case 1, (b) Case 2, and (c) Case 3 simulated with different scenarios of autoX-MCM. The measurements of the flow-tube reactors are shown in the horizontal black lines. The yellow shadow indicates the error range.

Table 7 Performance of oligomerization parameterization and the estimated oligomerization rate on the molar ratio of monomer and dimer (Case 5, before NO$_2$ injection 5a, and after NO$_2$ injection 5b; Case 6 (273 K), before NO$_2$ injection 6a, and after NO$_2$ injection 6b; Case 7 (313 K), before NO$_2$ injection 7a, and after NO$_2$ injection 7b). The signals of trimeric products are not included

	298 K 5a	298 K 5b	273 K 6a	273 K 6b	313 K 7a	313 K 7b
Gao et al.[6]	2.89	2.76	6.10	5.84	2.46	2.26
wo-oligo	26.4	6.55	30.7	13.8	9.35	4.2
w-oligo	2.89	1.96	6.10	5.24	2.46	1.02
w-oligo (no Oligomer-N)	2.89	2.65	6.10	5.81	2.46	2.12
r_{oligo} (s^{-1})	3.33×10^{-4}		5.99×10^{-5}		1.13×10^{-3}	
Fitted r_{oligo} (s^{-1})	3.33×10^{-4}		6.00×10^{-5}		8.16×10^{-4}	
Relative error (%)	0.00		0.16		27.74	
Estimated ratio	2.89	2.65	6.09	5.80	3.06	2.80

because the change of most parameters in the flow-tube experiments generally affects the ELVOC yield within the uncertainties of measurements.

3.4.3 Oligomerization. While the autoX-MCM includes RO$_2^\bullet \cdot$RO$_2^\bullet$ dimerization, the simulations revealed a significant discrepancy between simulated and measured SOA oligomer composition by Gao et al.[6] As shown by Table 7 illustrating the measured and simulated molar monomer on dimer ratio ($r_{m/d}$), the model significantly underestimated dimer concentrations (overestimation of $r_{m/d}$). For instance, in Case 5a, the simulated $r_{m/d}$ is 26.4, in contrast to the chamber measurements of 2.89 by Gao et al.,[6] who reported substantial fractions of dimeric and trimeric products (31.1% in Case 5a). These findings suggest that gas-phase chemistry alone is insufficient to reproduce the observed chemical complexity of SOA, indicating the need for particle-phase processes, most notably particle-phase oligomerization, to be included in the simulations.

To investigate the role of condensed-phase reactions, the bulk oligomerization parameterization of Couvidat et al.[44] was used to include the formation of dimers by particle-phase oligomerization. Two simulation sets were conducted: one excluding ('wo-oligo') and one including ('w-oligo') particle-phase oligomerization. The resulting SOA composition in terms of $r_{m/d}$, as well as total volume concentrations, were compared between the two simulations. Monomers were defined as products with carbon numbers C$_{1-15}$, while dimers spanned the range of C$_{16-30}$.

For the three experiments of Gao et al.,[6] the inclusion of oligomerization led to a substantial reduction in $r_{m/d}$, for instance, decreasing it (pre-NO$_2$ period) from 26.4 to 2.89 at 298 K, thereby bringing model simulations into much better agreement with experiments (Table 7). The oligomerization rate constants (r_{oligo}) were optimized by fitting to the $r_{m/d}$ values during the BCARY + O$_3$ (pre-NO$_2$ injection) period. To provide a physically meaningful temperature dependence for the oligomerization rate constant, the three optimized values of different temperatures (Table 7) were fitted to the Arrhenius equation:

$$k_{oligo}(T) = 4.47 \times 10^4 \times \exp\left(-\frac{46368}{RT}\right) \qquad (3)$$

with R the universal gas constant, T the temperature (in K), and $k_{oligo}(T)$ the kinetic of oligomerization in s^{-1} as a function of temperature. Using 3, the determined oligomerization rate constant at 293 K (2.4×10^{-4} s^{-1}) is very close to the

oligomerization rate constant proposed by Couvidat et al.[44] based on the evolution of the mass spectra measured at 293 K by Kalberer et al.[46] for isoprene and trimethylbenzene SOA (2.2×10^{-4} s^{-1}).

As shown in Table 7, a comparison between the BCARY + O$_3$ (pre-NO$_2$) and BCARY + NO$_3^\bullet$ (post-NO$_2$) regimes revealed regime-dependent differences in the dominant oligomer formation pathways. In the BCARY + O$_3$ case, the 'wo-oligo' simulation resulted in high $r_{m/d}$ values, confirming that gas-phase reactions alone could not account for the observed dimer fraction at all temperatures (e.g., dimers formed by gas-phase reactions contribute only to 6.6% to SOA concentrations compared with 31.1% of oligomers in SOA observed by Gao et al.[6] in the chamber at 298 K). However, in the post-NO$_2$ stage, 'wo-oligo' showed that a significant mass fraction of dimeric org-N (6.34% at 273 K, 11.93% at 298 K, and 16.79% at 313 K) was formed via gas-phase dimerization (C$_{30}$H$_{47}$O$_8$NO$_3$), aligning remarkably well with the experimental dimeric org-N molar fractions reported by Gao et al.[6] (4% at 273 K, 11% at 298 K, and 13% at 313 K, respectively). This suggests that the experimental dimeric org-N formation can largely be explained by gas-phase chemistry.

When particle-phase oligomerization ('w-oligo') was subsequently applied without distinguishing between nitrated (org-N) and non-nitrated compounds, the model generally overestimated the total dimer concentrations in the post-NO$_2$ regime, with simulated values at 298 K and 313 K being lower than measurements by a factor of approximately two. This overestimation was particularly evident for org-N dimers, with simulated molar fraction reaching 18% at 298 K, higher than the observed 11%. This discrepancy suggests that the fitted oligomerization kinetics might be too important for org-Ns, or that they are not subject to oligomerization. A third simulation set, 'w-oligo (no Oligomer-N)', was conducted in order to account for oligomerization for compounds without a nitrate group. As demonstrated in Table 7, this approach significantly improved the agreement with experiments in the post-NO$_2$ regimes (e.g., 2.65, closer to the observed 2.76 at 298 K).

Although oligomerization significantly alters the chemical composition of SOA, it has a limited impact on total SOA. As shown in Fig. S1, simulations conducted at three temperatures with and without oligomerization parameterization revealed only minor differences in volume concentrations. For example,

Table 8 Measured and simulated BCA yield in (%) for Case 5 (298 K) and Case 6 (273 K), before NO_2 injection

	Gao et al.[6]	autoX-MCM	mMCM
298 K	0.8 ± 0.5	0.78	0.65
313 K	0.6 ± 0.4	0.42	0.10
273 K	4.1 ± 2.7	0.68	0.70

at 228 min in Case 298 K, the 'w-oligo (no oligomer-N)' simulation yielded 46.04 nL m^{-3}, which is 2.74 nL m^{-3} lower than the 'w-oligo' simulation, and closely matches the measurement of 45.74 nL m^{-3}.[6] This result shows that the overall SOA loading is largely driven by the gas-phase chemistry and condensation of low-volatility products, while oligomerization primarily redistributes SOA between monomer and dimer species.

3.5 β-caryophyllinic acid yield

β-Caryophyllinic acid (BCA, C137CO2H (name in MCMv3.3.1)) is a characteristic oxidation product often used as a marker[6,47] of BCARY SOA. BCA is a low-volatility organic compound (LVOC), partitioning between the gas and particle phase, with an estimated saturation vapor pressure (using the 'v0b0' method) of approximately 3.95×10^{-8} torr. The most important BCA formation pathways in the MCMv3.3.1 are shown in Fig. S3. The particle-phase BCA concentrations simulated by the mMCM and autoX-MCM mechanisms were compared with the experimental BCA concentrations reported by Gao et al.[6]

As shown in Table 8, using autoX-MCM led to an improvement in simulating the yield of BCA compared to the mMCM. At 298 K, both mechanisms performed reasonably well. The most significant improvement offered by the autoX-MCM was observed at the high temperature of 313 K. A BCA yield of 0.42% was obtained with autoX-MCM (within the experimental uncertainty range of 0.6 ± 0.4%), while concentrations of BCA are lower by a factor of 4 with mMCM. The improvement of BCA concentrations at 313 K when using autoX-MCM is linked to the gas-particle partitioning. Indeed, at 298 K, BCA can be considered to be low-volatile and is almost entirely in the particle for both mMCM (97.1%) and autoX-MCM (98.7%). However, at 313 K, BCA should be considered a semi-volatile, and a significant fraction of BCA can remain in the gas-phase, especially in the early stage of the experiment. As shown in Fig. 3, the mMCM mechanism using 'v0b0' significantly underestimated SOA concentrations through all the experiments. Compared to the autoX-MCM, for which a large part of BCA is present in the particle (74.0%), only a fraction of BCA condenses in the particle due to the low SOA concentrations available (34.6%).

While the model performed reasonably well at 298 K and 313 K (within the uncertainties of measurements), the model failed to reproduce the very high BCA yields reported by Gao et al.[6] at 273 K (4.1% in measurements against 0.58% with autoX-MCM). Such a high yield of BCA cannot be explained with the current MCMv3.3.1, as the maximum theoretical yield is around 1%. This discrepancy could be explained by several reasons:

• An overestimation in the BCA yield reported by Gao et al.[6] at 273 K, for example, due to the detection of isomers.

• Missing processes occurring at very low temperatures that are not accounted for in the model (for example, heterogeneous reactions).

• Missing temperature-dependence of some reactions.

4 Conclusions

This study introduces the autoX-MCM, a chemical mechanism designed to simulate SOA formation and composition from the oxidation of BCARY by O_3 and $NO_3^\bullet$. The developed mechanism includes an autoxidation scheme constrained and validated against a suite of laboratory experiments available in the literature and conducted in various reactors. Our comprehensive evaluation demonstrates that the autoX-MCM significantly improves model performance compared to the original mMCM mechanism, particularly in reproducing ELVOC yields, SOA loading, new particle formation rates, and SOA composition.

Representing ELVOC formation and NPF is essential for accurately simulating SOA dynamics for the chamber experiment of Gao et al.[6] Indeed, the mMCM that does not include ELVOC formation by autoxidation failed to accurately reproduce SOA formation. Moreover, adding ELVOC formation by autoxidation leads to a better reproduction of the initial SOA growth and number concentration peaks for the experiment of Gao et al.[6] at all simulated temperature conditions (e.g., RMSE on SOA volume concentrations reduces from 4.81 to 0.53 nL m^{-3} during stage 1 at 298 K). For BCARY + $NO_3^\bullet$, the autoX-MCM mechanism manages to reproduce the rapid increase in SOA loading by assuming left-scission of the nitroxy-alkoxy radical $C_{15}H_{24}ONO_3^\bullet$ (denoted as 'NBCO' in the MCM mechanism) followed by autoxidation.

A complete evaluation of the SOA composition was also performed. SOA composition is found to be strongly affected by particle-phase oligomerization as oligomers represent more than 60% of non-nitrated SOA at all temperatures. Conversely, the sensitivity test strongly suggests that organic nitrate dimers are formed through gas-phase dimerization and are not subject to particle-phase oligomerization.

The autoX-MCM manages to reproduce the formation of BCA at 298 K and 313 K but the simulated BCA yield at 273 K is underestimated by nearly a factor of 4. The autoX-MCM also reproduces the organic nitrate (org-N) mass fraction (simulated fraction of 63.00%, which is in excellent agreement with the measured value of 58.96% from Gao et al.[6]).

The sensitivity analysis performed in this study provides critical insights into the autoX-MCM's robustness and sources of uncertainty. The model accuracy is notably influenced by the choice of P_{sat} estimation methods; different methods can lead to a four-fold range in simulated SOA loading. The sensitivity analysis indicates the P_{sat} estimation method of Myrdal and Yalkowsky[36] and Nannoolal et al.[38] ('v0b0') provides the best performance for the autoX-MCM. Furthermore, the autoxidation mechanism is found to be robust as the model of SOA loading exhibits strong sensitivity only to the initial stoichiometric yield of autoxidation-initiating peroxy radicals and the oxidation rate of BCARY by the $NO_3^\bullet$ radical.

Author contributions

YS, FC, and KS conceptualized the research. YS, FC, VL, and KS developed the methodology. YS and FC conducted the formal analysis. YS analyzed and visualized the study data. YS wrote the manuscript with contributions from FC, VL, and KS. FC and KS supervised the research. FC, VL, and KS contributed to the software development.

Conflicts of interest

There are no conflicts to declare.

Data availability

The source code for SSH-aerosol v2.0 is hosted on GitHub at https://github.com/sshaerosol/ssh-aerosol (last access: 05 February 2025). The dataset that we used to run the autoX-MCM and mMCM mechanisms is publicly available online on Zenodo: https://doi.org/10.5281/zenodo.17226329 (Shi *et al.*, 2025).

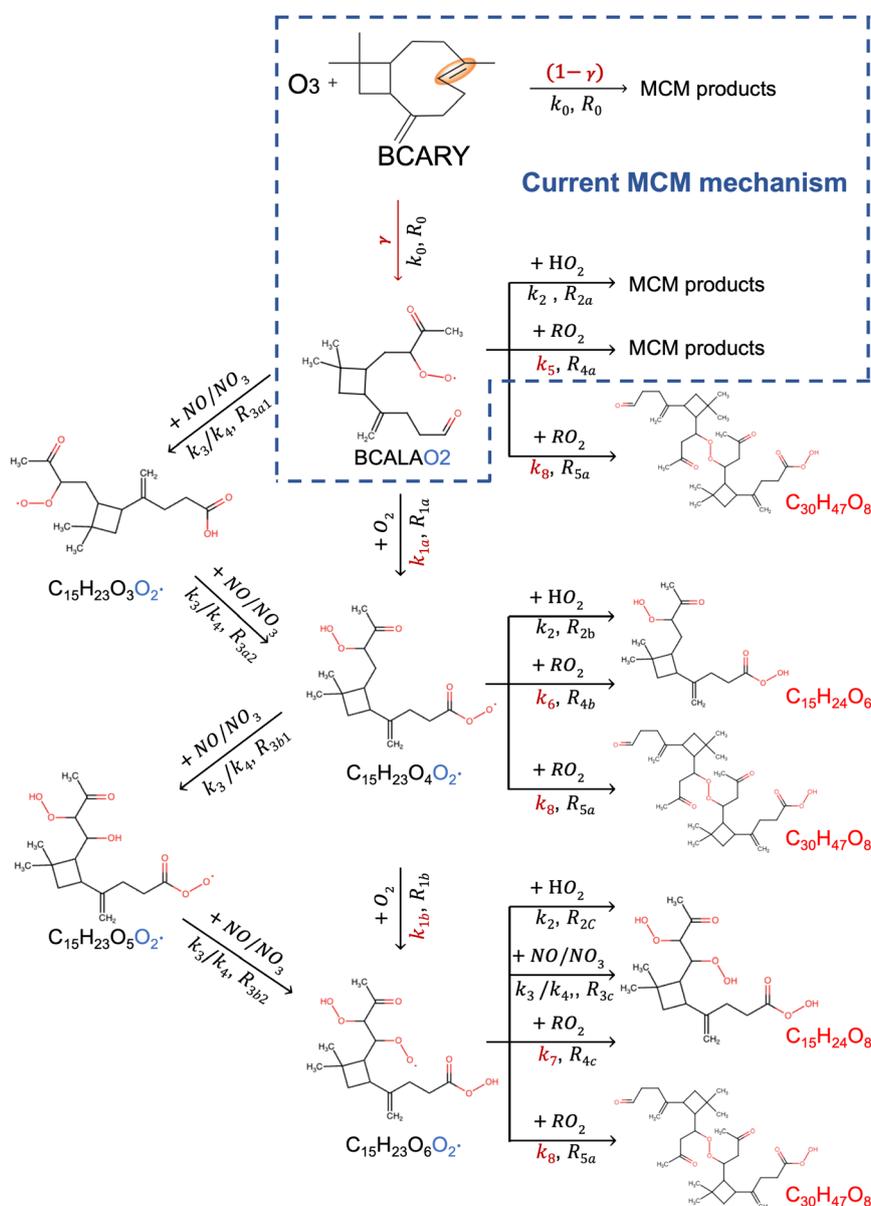Supplementary information (SI): the description of the main developments of autoX-MCM mechanism and addtional results. See DOI: https://doi.org/10.1039/d5ea00133a.

Fig. 6 Schematic representation of the gas-phase oxidation mechanism of BCARY initiated by O_3, highlighting the key autoxidation steps included in autoX-MCM. Parameters shown in red (*e.g.*, stoichiometric coefficients and rate constants) were optimized using experimental data, while those in black follow the default values from MCMv3.3.1. This figure illustrates the gas-phase formation of ELVOC precursors; subsequent gas-phase processes are not depicted.
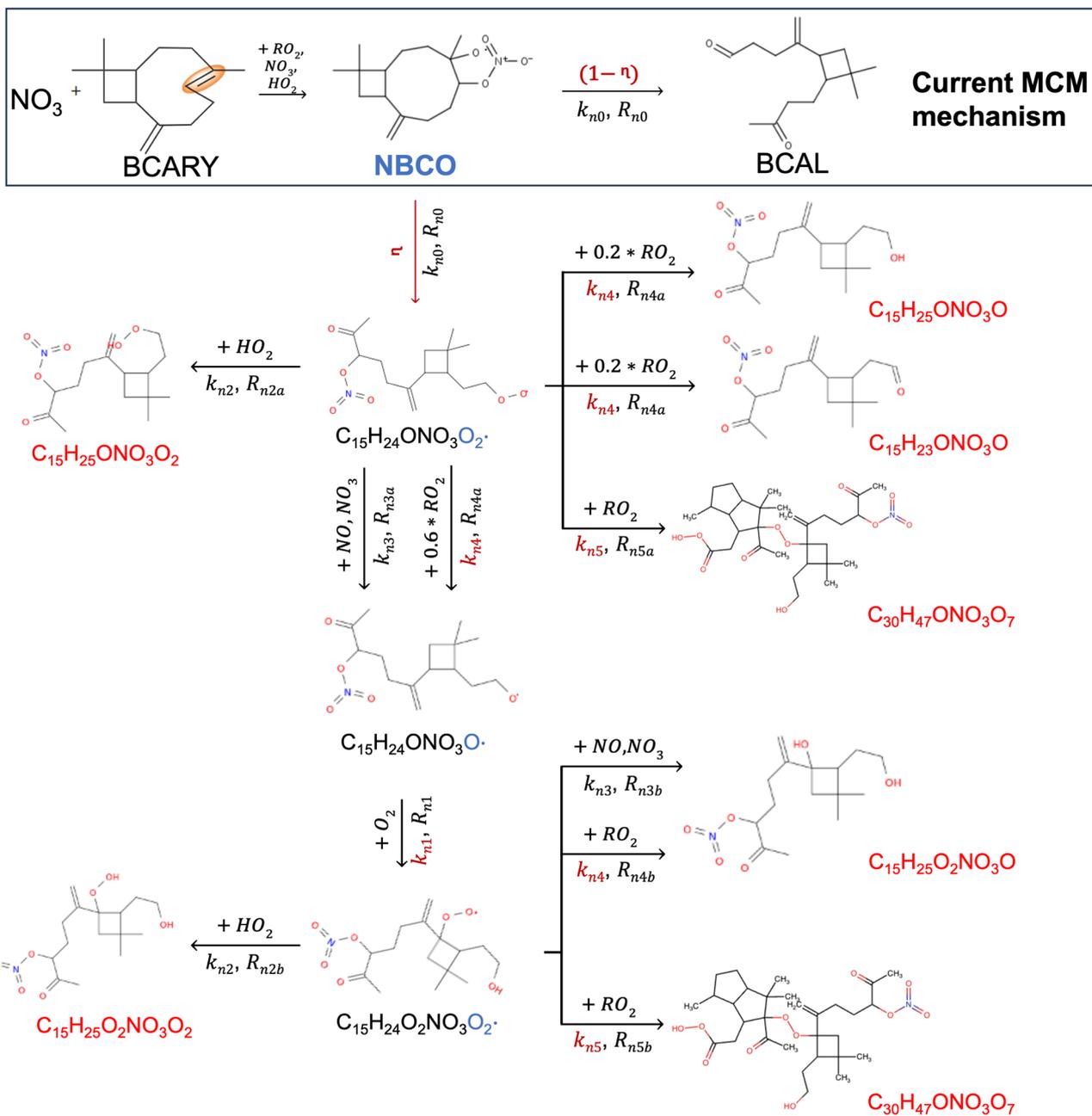
Fig. 7 Schematic representation of the gas-phase oxidation of BCARY initiated by $NO_3^•$, as incorporated in autoX-MCM. Parameters in red are adapted from the $NO_3^•$ autoxidation pathway; black parameters are consistent with MCMv3.3.1. $RO_2^•$ structures and representative products are derived from GECKO-A. The mechanism focuses on ELVOC formation in the gas phase and does not include particle-phase processes.

Appendix

Fig. 6 and 7 provide schematic representations of the ELVOC formation pathways from BCARY oxidation initiated by O_3 and $NO_3^•$, respectively.

Acknowledgements

References

1 A. Guenther, X. Jiang, C. L. Heald, T. Sakulyanontvittaya, T. a. Duhl, L. Emmons and X. Wang, The Model of Emissions of Gases and Aerosols from Nature version 2.1 (MEGAN2. 1): an extended and updated framework for modeling biogenic emissions, *Geosci. Model Dev.*, 2012, **5**, 1471–1492.

2 H. Hellén, A. P. Praplan, T. Tykkä, I. Ylivinkka, V. Vakkari, J. Bäck, T. Petäjä, M. Kulmala and H. Hakola, Long-term measurements of volatile organic compounds highlight the

importance of sesquiterpenes for the atmospheric chemistry of a boreal forest, *Atmos. Chem. Phys.*, 2018, **18**, 13839–13863.

3 L. M. Barreira, A. Ylisirniö, I. Pullinen, A. Buchholz, Z. Li, H. Lipp, H. Junninen, U. Hõrrak, S. M. Noe, A. Krasnova, D. Krasnov, K. Kask, E. Talts, Ü. Niinemets, J. Ruiz-Jimenez and S. Schobesberger, The importance of sesquiterpene oxidation products for secondary organic aerosol formation in a springtime hemiboreal forest, *Atmos. Chem. Phys.*, 2021, **21**, 11781–11800.

4 P. Fu, K. Kawamura, J. Chen and L. A. Barrie, Isoprene, monoterpene, and sesquiterpene oxidation products in the high Arctic aerosols during late winter to early summer, *Environ. Sci. Technol.*, 2009, **43**, 4022–4028.

5 A. Lee, A. H. Goldstein, J. H. Kroll, N. L. Ng, V. Varutbangkul, R. C. Flagan and J. H. Seinfeld, Gas-phase products and secondary aerosol yields from the photooxidation of 16 different terpenes, *J. Geophys. Res. Atmos.*, 2006, **111**, D17305.

6 L. Gao, J. Song, C. Mohr, W. Huang, M. Vallon, F. Jiang, T. Leisner and H. Saathoff, Kinetics, SOA yields, and chemical composition of secondary organic aerosol from β-caryophyllene ozonolysis with and without nitrogen oxides between 213 and 313 K, *Atmos. Chem. Phys.*, 2022, **22**, 6001–6020.

7 M. Shrivastava, M. O. Andreae, P. Artaxo, H. M. Barbosa, L. K. Berg, J. Brito, J. Ching, R. C. Easter, J. Fan and J. D. Fast, others Urban pollution greatly enhances formation of natural aerosols over the Amazon rainforest, *Nat. Commun.*, 2019, **10**, 1046.

8 H. Zhang and Q. Ying, Secondary organic aerosol formation and source apportionment in Southeast Texas, *Atmos. Environ.*, 2011, **45**, 3217–3227.

9 M. Khan, M. Jenkin, A. Foulds, R. Derwent, C. Percival and D. Shallcross, A modeling study of secondary organic aerosol formation from sesquiterpenes using the STOCHEM global chemistry and transport model, *J. Geophys. Res. Atmos.*, 2017, **122**, 4426–4439.

10 R. Winterhalter, F. Herrmann, B. Kanawati, T. L. Nguyen, J. Peeters, L. Vereecken and G. K. Moortgat, The gas-phase ozonolysis of β-caryophyllene ($C_{15} H_{24}$). Part I: an experimental study, *Phys. Chem. Chem. Phys.*, 2009, **11**, 4152–4172.

11 T. L. Nguyen, R. Winterhalter, G. Moortgat, B. Kanawati, J. Peeters and L. Vereecken, The gas-phase ozonolysis of β-caryophyllene (C 15 H 24). Part II: A theoretical study, *Phys. Chem. Chem. Phys.*, 2009, **11**, 4173–4183.

12 L. Dada, D. Stolzenburg, M. Simon, L. Fischer, M. Heinritzi, M. Wang, M. Xiao, A. L. Vogel, L. Ahonen, A. Amorim, R. Baalbaki, A. Baccarini, U. Baltensperger, F. Bianchi, K. R. Daellenbach, J. DeVivo, A. Dias, J. Dommen, J. Duplissy, H. Finkenzeller, A. Hansel, X.-C. He, V. Hofbauer, C. R. Hoyle, J. Kangasluoma, C. Kim, A. Kürten, A. Kvashnin, R. Mauldin, V. Makhmutov, R. Marten, B. Mentler, W. Nie, T. Petäjä, L. L. J. Quéléver, H. Saathoff, C. Tauber, A. Tome, U. Molteni, R. Volkamer, R. Wagner, A. C. Wagner, D. Wimmer, P. M. Winkler, C. Yan, Q. Zha, M. Rissanen, H. Gordon, J. Curtius, D. R. Worsnop, K. Lehtipalo, N. M. Donahue, J. Kirkby,

I. El Haddad and M. Kulmala, Role of sesquiterpenes in biogenic new particle formation, *Sci. Adv.*, 2023, **9**, eadi5297.

13 G. Isaacman-VanWertz, G. Frazier, J. Willison and C. Faiola, Missing measurements of sesquiterpene ozonolysis rates and composition limit understanding of atmospheric reactivity, *Environ. Sci. Technol.*, 2024, **58**, 7937–7946.

14 T. Jokinen, O. Kausiala, O. Garmash, O. Peräkylä, H. Junninen, S. Schobesberger, C. Yan, M. Sipilä and M. P. Rissanen, Production of highly oxidized organic compounds from ozonolysis of β-caryophyllene: laboratory and field measurements, *Boreal Environ. Res.*, 2016, **21**, 262.

15 S. Richters, H. Herrmann and T. Berndt, Different pathways of the formation of highly oxidized multifunctional organic compounds (HOMs) from the gas-phase ozonolysis of β-caryophyllene, *Atmos. Chem. Phys.*, 2016, **16**, 9831–9845.

16 S. Richters, H. Herrmann and T. Berndt, Highly oxidized RO2 radicals and consecutive products from the ozonolysis of three sesquiterpenes, *Environ. Sci. Technol.*, 2016, **50**, 2354–2362.

17 A. Fouqueau, M. Cirtog, M. Cazaunau, E. Pangui, J.-F. Doussin and B. Picquet-Varrault, An experimental study of the reactivity of terpinolene and β-caryophyllene with the nitrate radical, *Atmos. Chem. Phys.*, 2022, **22**, 6411–6434.

18 F. Bianchi, T. Kurtén, M. Riva, C. Mohr, M. P. Rissanen, P. Roldin, T. Berndt, J. D. Crounse, P. O. Wennberg, T. F. Mentel, J. Wildt, H. Junninen, T. Jokinen, M. Kulmala, D. R. Worsnop, J. A. Thornton, N. Donahue, H. G. Kjaergaard and M. Ehn, Highly oxygenated organic molecules (HOM) from gas-phase autoxidation involving peroxy radicals: A key contributor to atmospheric aerosol, *Chem. Rev.*, 2019, **119**, 3472–3509.

19 M. Ehn, J. A. Thornton, E. Kleist, M. Sipilä, H. Junninen, I. Pullinen, M. Springer, F. Rubach, R. Tillmann and B. Lee, others A large source of low-volatility secondary organic aerosol, *Nature*, 2014, **506**, 476–479.

20 T. Jokinen, T. Berndt, R. Makkonen, V.-M. Kerminen, H. Junninen, P. Paasonen, F. Stratmann, H. Herrmann, A. B. Guenther, D. R. Worsnop, M. Kulmala, M. Ehn and M. Sipilä, *Production of Extremely Low Volatile Organic Compounds from Biogenic Emissions: Measured Yields and Atmospheric Implications*, Proceedings of the National Academy of Sciences, 2015, vol. 112, pp. 7123–7128.

21 P. Roldin, M. Ehn, T. Kurtén, T. Olenius, M. P. Rissanen, N. Sarnela, J. Elm, P. Rantala, L. Hao, N. Hyttinen, L. Heikkinen, D. R. Worsnop, L. Pichelstorfer, C. Xavier, P. Clusius, E. Öström, T. Petäjä, M. Kulmala, H. Vehkamäki, A. Virtanen, I. Riipinen and M. Boy, The role of highly oxygenated organic molecules in the Boreal aerosol-cloud-climate system, *Nat. Commun.*, 2019, **10**, 4370.

22 X. Shao, M. Wang, X. Dong, Y. Liu, W. Shen, S. R. Arnold, L. A. Regayre, M. O. Andreae, M. L. Pöhlker, D. S. Jo, M. Yue and K. S. Carslaw, Global modeling of aerosol nucleation with a semi-explicit chemical mechanism for highly oxygenated organic molecules (HOMs), *Atmos. Chem. Phys.*, 2024, **24**, 11365–11389.

23 Z. Wang, F. Couvidat and K. Sartelet, Response of biogenic secondary organic aerosol formation to anthropogenic NOx emission mitigation, *Sci. Total Environ.*, 2024, **927**, 172142.

24 M. Chrit, K. Sartelet, J. Sciare, J. Pey, N. Marchand, F. Couvidat, K. Sellegri and M. Beekmann, Modelling organic aerosol concentrations and properties during ChArMEx summer campaigns of 2012 and 2013 in the western Mediterranean region, *Atmos. Chem. Phys.*, 2017, **17**, 12509–12531.

25 K. Sengupta, K. Pringle, J. S. Johnson, C. Reddington, J. Browse, C. E. Scott and K. Carslaw, A global model perturbed parameter ensemble study of secondary organic aerosol formation, *Atmos. Chem. Phys.*, 2021, **21**, 2693–2723.

26 K. Sartelet, F. Couvidat, Z. Wang, C. Flageul and Y. Kim, SSH-aerosol v1. 1: A modular box model to simulate the evolution of primary and secondary aerosols, *Atmosphere*, 2020, **11**, 525.

27 K. Sartelet, Z. Wang, Y. Kim, V. Lannuque and F. Couvidat, Advanced modeling of gas chemistry and aerosol dynamics with SSH-aerosol v2.0, *EGUsphere*, 2025, **2025**, 1–41.

28 G. Yarwood, S. Rao, M. Yocke and G. Whitten, *Updates to the Carbon Bond Chemical Mechanism: CB05*, Final Report prepared for US EPA, 2005.

29 M. Jenkin, K. Wyche, C. Evans, T. Carr, P. Monks, M. Alfarra, M. Barley, G. McFiggans, J. Young and A. Rickard, Development and chamber evaluation of the MCM v3. 2 degradation scheme for β-caryophyllene, *Atmos. Chem. Phys.*, 2012, **12**, 5275–5308.

30 G. M. Lanzafame, B. Bessagnet, D. Srivastava, J. L. Jaffrezo, O. Favez, A. Albinet and F. Couvidat, Modelling aerosol molecular markers in a 3D air quality model: Focus on anthropogenic organic markers, *Sci. Total Environ.*, 2022, **835**, 155360.

31 S. Zhu, K. N. Sartelet and C. Seigneur, A size-composition resolved aerosol model for simulating the dynamics of externally mixed particles: SCRAM (v 1.0), *Geosci. Model Dev. Discuss.*, 2014, **7**, 7937–7987.

32 F. Couvidat and K. Sartelet, The Secondary Organic Aerosol Processor (SOAP v1. 0) model: a unified model with different ranges of complexity based on the molecular surrogate approach, *Geosci. Model Dev.*, 2015, **8**, 1111–1138.

33 D. Topping, M. Barley, M. K. Bane, N. Higham, B. Aumont, N. Dingle and G. McFiggans, UManSysProp v1.0: an online and open-source facility for molecular property prediction and atmospheric aerosol calculations, *Geosci. Model Dev.*, 2016, **9**, 899–914.

34 S. Compernolle, K. Ceulemans and J.-F. Müller, EVAPORATION: a new vapour pressure estimation method for organic molecules including non-additivity and intramolecular interactions, *Atmos. Chem. Phys.*, 2011, **11**, 9431–9450.

35 J. F. Pankow and W. E. Asher, SIMPOL. 1: a simple group contribution method for predicting vapor pressures and enthalpies of vaporization of multifunctional organic compounds, *Atmos. Chem. Phys.*, 2008, **8**, 2773–2796.

36 P. B. Myrdal and S. H. Yalkowsky, Estimating pure component vapor pressures of complex organic molecules, *Ind. Eng. Chem. Res.*, 1997, **36**, 2494–2499.

37 Y. Nannoolal, J. Rarey and D. Ramjugernath, Estimation of pure component properties: Part 3. Estimation of the vapor pressure of non-electrolyte organic compounds via group contributions and group interactions, *Fluid Phase Equilib.*, 2008, **269**, 117–133.

38 Y. Nannoolal, J. Rarey, D. Ramjugernath and W. Cordes, Estimation of pure component properties: Part 1. Estimation of the normal boiling point of non-electrolyte organic compounds via group contributions and group interactions, *Fluid Phase Equilib.*, 2004, **226**, 45–63.

39 S. E. Stein and R. L. Brown, Estimation of normal boiling points from group contributions, *J. Chem. Inf. Comput. Sci.*, 1994, **34**, 581–587.

40 K. G. Joback and R. C. Reid, Estimation of pure-component properties from group-contributions, *Chem. Eng. Commun.*, 1987, **57**, 233–243.

41 K. Sartelet, Y. Kim, F. Couvidat, M. Merkel, T. Petäjä, J. Sciare and A. Wiedensohler, Influence of emission size distribution and nucleation on number concentrations over Greater Paris, *Atmos. Chem. Phys. Discuss.*, 2022, **22**, 8579–8596.

42 H. Saathoff, K.-H. Naumann, O. Möhler, Å. M. Jonsson, M. Hallquist, A. Kiendler-Scharr, T. F. Mentel, R. Tillmann and U. Schurath, Temperature dependence of yields of secondary organic aerosols from the ozonolysis of α-pinene and limonene, *Atmos. Chem. Phys.*, 2009, **9**, 1551–1577.

43 M. Kuwata, S. R. Zorn and S. T. Martin, Using elemental ratios to predict the density of organic material composed of carbon, hydrogen, and oxygen, *Environ. Sci. Technol.*, 2012, **46**, 787–794.

44 F. Couvidat, M. G. Vivanco and B. Bessagnet, Simulating secondary organic aerosol from anthropogenic and biogenic precursors: comparison to outdoor chamber experiments, effect of oligomerization on SOA formation and reactive uptake of aldehydes, *Atmos. Chem. Phys.*, 2018, **18**, 15743–15766.

45 B. Zhao, N. M. Donahue, K. Zhang, L. Mao, M. Shrivastava, P.-L. Ma, J. Shen, S. Wang, J. Sun, H. Gordon, S. Tang, J. Fast, M. Wang, Y. Gao, C. Yan, B. Singh, Z. Li, L. Huang, S. Lou, G. Lin, H. Wang, J. Jiang, A. Ding, W. Nie, X. Qi, X. Chi and L. Wang, Global variability in atmospheric new particle formation mechanisms, *Nature*, 2024, **631**, 98–105.

46 M. Kalberer, D. Paulsen, M. Sax, M. Steinbacher, J. Dommen, A. S. H. Prevot, R. Fisseha, E. Weingartner, V. Frankevich, R. Zenobi and U. Baltensperger, Identification of Polymers as Major Components of Atmospheric Organic Aerosols, *Science*, 2004, **303**, 1659–1662.

47 M. Jaoui, M. Lewandowski, T. E. Kleindienst, J. H. Offenberg and E. O. Edney, β-caryophyllinic acid: An atmospheric tracer for β-caryophyllene secondary organic aerosol, *Geophys. Res. Lett.*, 2007, **34**, L05816.